

## **PAPER**

# 3D bioprinting of dense cellular structures within hydrogels with spatially controlled heterogeneity

To cite this article: Alperen Abaci and Murat Guvendiren 2024 Biofabrication 16 035027

View the article online for updates and enhancements.

# You may also like

- 3D coaxial bioprinting: process mechanisms, bioinks and applications Tarun Shyam Mohan, Pallab Datta, Sepehr Nesaei et al.
- Recent advancements in the bioprinting of vascular grafts
   Faraz Fazal, Sakshika Raghav, Anthony Callanan et al.
- Bioprinted in vitro tissue models: an emerging platform for developing therapeutic interventions and disease modelling
  Nandana Bhardwaj, Souradeep Dey, Bibrita Bhar et al.

# **Biofabrication**



RECEIVED 17 April 2024

17 April 202

REVISED 21 May 2024

ACCEPTED FOR PUBLICATION

31 May 2024

PURIISHED

11 June 2024

#### PAPER

# 3D bioprinting of dense cellular structures within hydrogels with spatially controlled heterogeneity

Alperen Abaci<sup>1</sup> and Murat Guvendiren<sup>1,2,\*</sup>

- Otto H. York Chemical and Materials Engineering Department, New Jersey Institute of Technology, Newark, NJ, United States of America
- <sup>2</sup> Bioengineering Department, New Jersey Institute of Technology, Newark, NJ, United States of America
- \* Author to whom any correspondence should be addressed.

E-mail: muratg@njit.edu

Keywords: bioinks, embedded printing, human adult mesenchymal stem cells, stem cell differentiation, bone regeneration, tissue engineering

Supplementary material for this article is available online

### **Abstract**

Embedded bioprinting is an emerging technology for precise deposition of cell-laden or cell-only bioinks to construct tissue like structures. Bioink is extruded or transferred into a yield stress hydrogel or a microgel support bath allowing print needle motion during printing and providing temporal support for the printed construct. Although this technology has enabled creation of complex tissue structures, it remains a challenge to develop a support bath with user-defined extracellular mimetic cues and their spatial and temporal control. This is crucial to mimic the dynamic nature of the native tissue to better regenerate tissues and organs. To address this, we present a bioprinting approach involving printing of a photocurable viscous support layer and bioprinting of a cell-only or cell-laden bioink within this viscous layer followed by brief exposure to light to partially crosslink the support layer. This approach does not require shear thinning behavior and is suitable for a wide range of photocurable hydrogels to be used as a support. It enables multi-material printing to spatially control support hydrogel heterogeneity including temporal delivery of bioactive cues (e.g. growth factors), and precise patterning of dense multi-cellular structures within these hydrogel supports. Here, dense stem cell aggregates are printed within methacrylated hyaluronic acid-based hydrogels with patterned heterogeneity to spatially modulate human mesenchymal stem cell osteogenesis. This study has significant impactions on creating tissue interfaces (e.g. osteochondral tissue) in which spatial control of extracellular matrix properties for patterned stem cell differentiation is crucial.

### 1. Introduction

Native tissue is composed of a dense cellular structure supported by an extracellular matrix (ECM). The ECM provides mechanical, topographical, and biochemical cues to regulate cellular functions, such as proliferation, migration, and differentiation. The cell-cell and cell-matrix interactions play crucial role during tissue development and disease. Thus, successful fabrication of a functional tissue requires manufacturing strategies that can recapitulate the native ECM along with precise assembly and patterning of cells into dense structures [1–5].

The emergence of extrusion-based embedded three-dimensional (3D) bioprinting approach

enabled fabrication of 3D complex geometries [6–10]. This approach involves extrusion of a bioink within a support medium that provides temporary support for the printed structure which is removed post-printing to leave behind the printed construct [11–13]. The commonly used support medium is composed of jammed microgel particles due to their shear thinning and recovery (self-healing) behavior [14–16]. The support medium displays a liquid-like behavior under shear during printing allowing needle motion, and immediately transforms into a stable solid-like structure when the shear is removed. This approach allows fabrication of soft tissue-like structures, with overhanging features and hollow channels, that are not possible to fabricate with conventional

extrusion-based 3D bioprinting technology [17–22]. However, the bioinks used in this approach are predominantly cell-laden hydrogels leading to limited cell-cell interactions and significantly lower cell densities when compared to the native tissue.

There is a recent paradigm shift in 3D bioprinting towards fabricating dense cellular structures to better recapitulate the physiology of the native tissue. In this regard, cell-only bioinks in the form of spheroids and aggregates have been used to create dense cellular structures. Aspiration assisted technologies have been developed for precise positioning of the spheroids into dense tissue constructs. This approach involves aspiration of a spheroid in a cell media reservoir followed by direct transfer of the spheroid into a temporary support medium and positioning of the spheroid within the support medium [23–29]. A magnetized 3D printing approach utilizing a magnetic nanoparticle-laden support hydrogel system was developed to precisely position organoids to generate assembloids [25]. The widespread utilization of these approaches is currently limited due to preprocessing time required to prepare spheroids, slow printing process, complicated instrumental setups, and necessary expertise to operate these bioprinters. Cell-only bioinks in the form of cell aggregates provide significant advantages as they can be directly extruded within a support medium while providing much higher deposition rates as compared to placing individual spheroids into tissue like structures [30–33].

Hydrogels have emerged as cell instructive microenvironments for embedded cells providing developmentally relevant cell-matrix interactions [34-41]. Cells feel their surrounding matrix and respond to the changes in the matrix heterogeneity by adjusting their functions including differentiation [42–44]. Although cell-only bioinks have been used in embedded bioprinting to create dense cellular structures within support hydrogels, most of these support hydrogels lack the physiologically relevant ECM heterogeneity to control cell function and act as a temporal support. To control cellular function, cells are usually pre-conditioned before printing. For instance, bone and cartilage tissues were bioprinted by culturing human adipose-derived stem cell spheroids in chondrogenic and osteogenic induction media (OM) before bioprinting [23]. The longer the stem cells were exposed to OM on 2D culture, the more pronounced was the osteogenic differentiation in spheroids as well as in the bioprinted tissues [23]. Healthy and fibrotic cardiac tissue spheroids were prepared to bioprint healthy and scarred myocardium tissue rings [26]. Cell spheroids and/or organoids were used to create a granular tissue matrix for embedded deposition of sacrificial hydrogels to create thick tissues with embedded channels for vascularization [10]. To provide prolonged tissue culture for embedded dense cellular structures (up to 4 weeks), Jeon et al

developed an oxidized methacrylated alginate (OMA) microgel support system [32]. OMA microgels are designed to photocrosslink post-printing to provide stability during culture and to degrade overtime for removal of the tissue construct [32]. A 4D bioprinting approach was developed to deposit hMSC aggregates within a shape morphing bilayer hydrogel disc to create dense chondrogenic structures with a preprogrammed shape [33]. Brassard et al bioprinted mesenchymal aggregates, intestinal organoids or vascular organoids within a Matrigel/collagen support and demonstrated the fabrication of self-organized macroscopic tissue mimetics including connective tissue, epithelial tissue, and vascular network [31]. Despite the recent advancements to design more functional support medium to direct cellular behavior post-printing, bioprinting dense cellular structures within ECM mimetic microenvironment with spatially and temporally controlled heterogeneity remains a challenge. This is particularly important to create tissue interfaces where spatial control of ECM properties and cellular behavior are crucial.

Here, we report a 3D bioprinting strategy to fabricate dense cellular structures within photocurable hydrogels with spatial and temporal control of cell-instructive cues. Our approach involves printing of a photocurable viscous hydrogel (support) layer and deposition of cell aggregates within this layer on demand. Viscosity of the hydrogel ink can be adjusted to allow needle motion and material extrusion within the printed hydrogel layer eliminating the need for shear thinning and recovery behavior. This expands the available hydrogel inks suitable for support medium. Our approach enables the use of a cell-instructive hydrogel as a support medium, which remains stable during long term culture to modulate cell behavior or is removed over time to leave behind cell-only constructs. Our approach allows the use of multiple hydrogel inks to create local matrix heterogeneity and bioprinting of different cell-only inks to create multi-cellular structures. To demonstrate the utility of this approach, we fabricate dense cellular structures within methacrylated hyaluronic acid (MeHA) hydrogels and report the effect of spatiotemporally controlled cell-instructive matrix heterogeneity on patterned stem cell osteogenesis. This approach is versatile and presents a significant advancement towards creating highly complex heterogenous micro tissues and tissue interfaces such as osteochondral interface.

# 2. Results and discussion

# 2.1. 3D bioprinting cell aggregates within functional hydrogels

We developed an extrusion-based 3D bioprinting approach to print cell aggregates and/or cell-laden hydrogels within photocurable functional hydrogels (figure 1). Our approach involves (i) printing of a

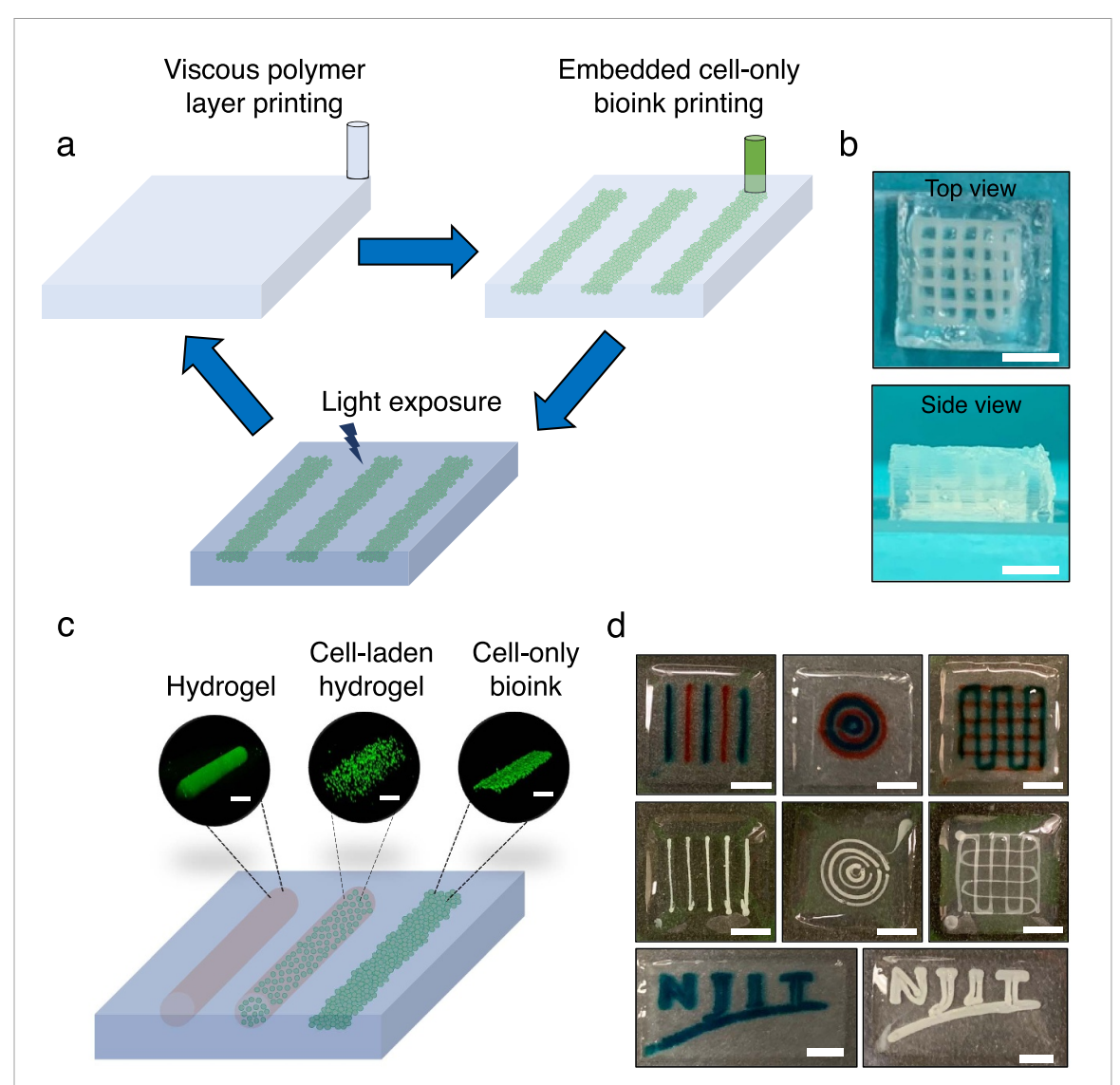


**Figure 1.** Bioprinting of dense cellular structures within functional hydrogels. (a) Schematic of bioprinting approach including printing of a viscous support layer, printing of cell aggregates into support layer, and partial curing. This process can be repeated to create 3D constructs. (b) Representative picture of a 3D construct with embedded dense cellular structure. Scale bars = 5 mm. (c) Schematic showing printing of an acellular hydrogel, a cell-laden hydrogel, and a cell-only bioink within hydrogel support. Top images show confocal images of the printed structures corresponding to the schematic. Hydrogel is loaded with fluorescent beads (green) and cells are stained with live/dead staining (green and red showing live and dead cells). (d) Pictures showing cell-laden MeHA (labeled with green or red food coloring) and cell-only (NIH3T3) constructs printed within MeAlg hydrogels. Scale bars = 5 mm.

viscous photocurable hydrogel ink to form a support layer, (ii) on demand deposition of cell aggregates or cell-laden hydrogels within this viscous support layer, and (iii) exposure of the support layer to light briefly (typically 5-15 s) to ensure formation of a partly crosslinked self-supporting layer (figure 1(a)). This process is repeated layer-by-layer to create a 3D construct, which is then exposed to light (up to 3 min) to fully crosslink the support hydrogel matrix (figures 1(b)-(d), movie S1, supporting information). Each printed support layer is typically 200–300  $\mu$ m in height but layer height can be easily controlled down to  $\sim$ 80  $\mu$ m to ensure direct contact between embedded structures without requiring print needle to penetrate within pre-crosslinked layers. The viscous support layer allows the motion of the print needle without the need for shear thinning behavior and ensures shape integrity of the printed structures. A wide range of commonly used photocurable hydrogel inks are suitable for support matrix as it is easy to adjust their viscosity by controlling the hydrogel concentration. This allows formation of a support matrix that is biologically inert, such as methacrylated alginate (MeAlg), or cell-instructive, such as MeHA, methacrylated heparin (MeHep) or carboxymethyl cellulose (CMC), which is discussed later.

To showcase the versatility and potential of our approach, we printed diverse array of 3D constructs (figure 2). These include a micro tissue composed of multiple layers of cell aggregates printed within MeHA matrix and dense cell strands printed within

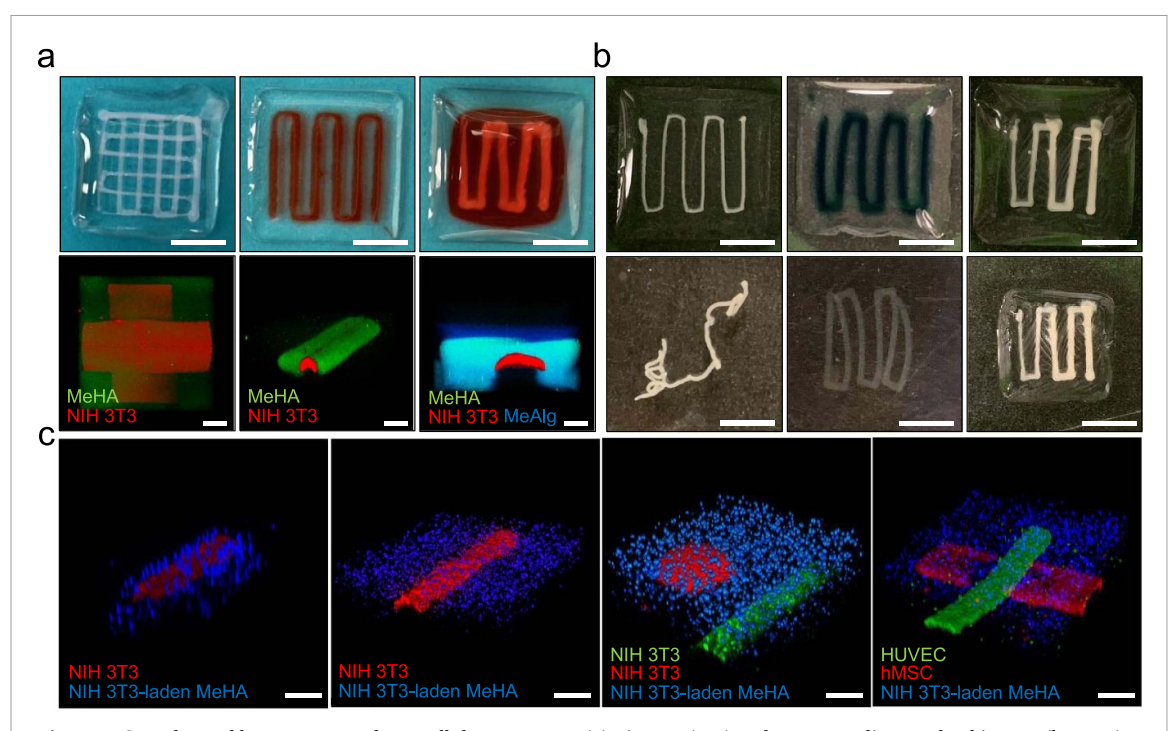


Figure 2. Complex and heterogeneous dense cellular structures. (a) Pictures (top) and corresponding confocal images (bottom) of embedded NIH3T3 constructs. From left to right, 3D NIH3T3 construct printed within MeHA hydrogel, continuous NIH3T3 strand printed within MeHA hydrogel strut embedded within MeAlg hydrogel, and continuous NIH3T3 strand printed within MeHA matrix embedded within MeAlg. MeHA hydrogel is labeled with red food coloring. For confocal imaging, MeHA and MeAlg are mixed with fluorescent beads (green) and DAPI, respectively. NIH3T3s are stained with rhodamine phalloidin. (b) Pictures of dense cell layers before (top) and after (bottom) removal of the cellulose-based support. From left to right, continuous NIH3T3 strand, cell-laden MeHA strut, and NIH3T3 strand within MeHA hydrogel embedded in cellulose-based removable support. (c) Confocal images of multi-cellular constructs. From left to right: NIH3T3 strand (red) printed within NIH3T3-laden MeHA support, NIH3T3 strand (green) and nodule (red) printed within NIH3T3-laden MeHA support, NIH3T3 strand (green) and nodule (red) printed within NIH3T3-laden MeHA support, NIH3T3 are labeled in blue for cell-laden MeHA. Scale bars are 200  $\mu$ m and 5 mm for confocal images and pictures, respectively.

MeHA matrix embedded within MeAlg matrix in the form of connecting struts or a cube (figure 2(a)). These support matrices provide long term stability as crosslinked MeHA and MeAlg are not degradable. A hydrolytically degradable carbic norbornene functionalized CMC (cCMC) was used as a temporary support to demonstrate the release of the printed structures over time. Cell-only strands, cellladen MeHA strands and dense cell strands embedded within MeHA matrix were obtained after 4 d of culture in vitro (figure 2(b)). This cCMC hydrogel bioink was developed previously to control degradation of the hydrogel by utilizing an ester linkage between norbornene functional group and HA backbone [45]. Although the overall shape of the cell-only print was scrambled due to single-layer design, the integrity of the strands was maintained confirming cell aggregate fusion within 4 d culture (figure 2(b)). For cell-laden design, MeHA matrix preserved the print shape postrelease by providing structural support (figure 2(b)). In addition to controlling matrix heterogeneity by printing different ink compositions sequentially or within each other, our approach also allows control of cellular heterogeneity by bioprinting different types of cell aggregates within a cell-laden support matrix (figure 2(c)). Overall, these examples show our ability

to create 3D micro tissues composed of dense multicellular structures enclosed within functional support matrices.

# 2.2. Effect of rheological properties of the bioinks on printability

Hydrogel ink rheology is important to determine the printability of the inks to form the viscous support layer and the suitability of this support layer for subsequent deposition of cell aggregates or cell-laden hydrogels. Firstly, the viscosity  $(\eta)$  of the support ink is critical in this approach and is constrained within 0.1-10 Pa.s range to allow the motion of the print needle within the support layer without the need for shear thinning behavior while maintaining the shape integrity of the printed structures (figure 3(a)). Increasing the polymer concentration from 10 to 20 wt% for MeAlg and from 5 to 15 wt% for MeHA led to inks with higher viscosity (figure 3(a)). Although 20 wt% MeAlg showed a shear thinning behavior indicated by a slight decrease in ink viscosity with shear rate, the other ink formulations behaved more like a Newtonian fluid (flow index values found from power-law model for 5%, 10%, and 15% MeHA are  $\sim$ 1.00, 0.97, and 0.95, respectively, and 10% and 20% MeAlg are  $\sim$ 0.96 and 0.78, respectively). The gel

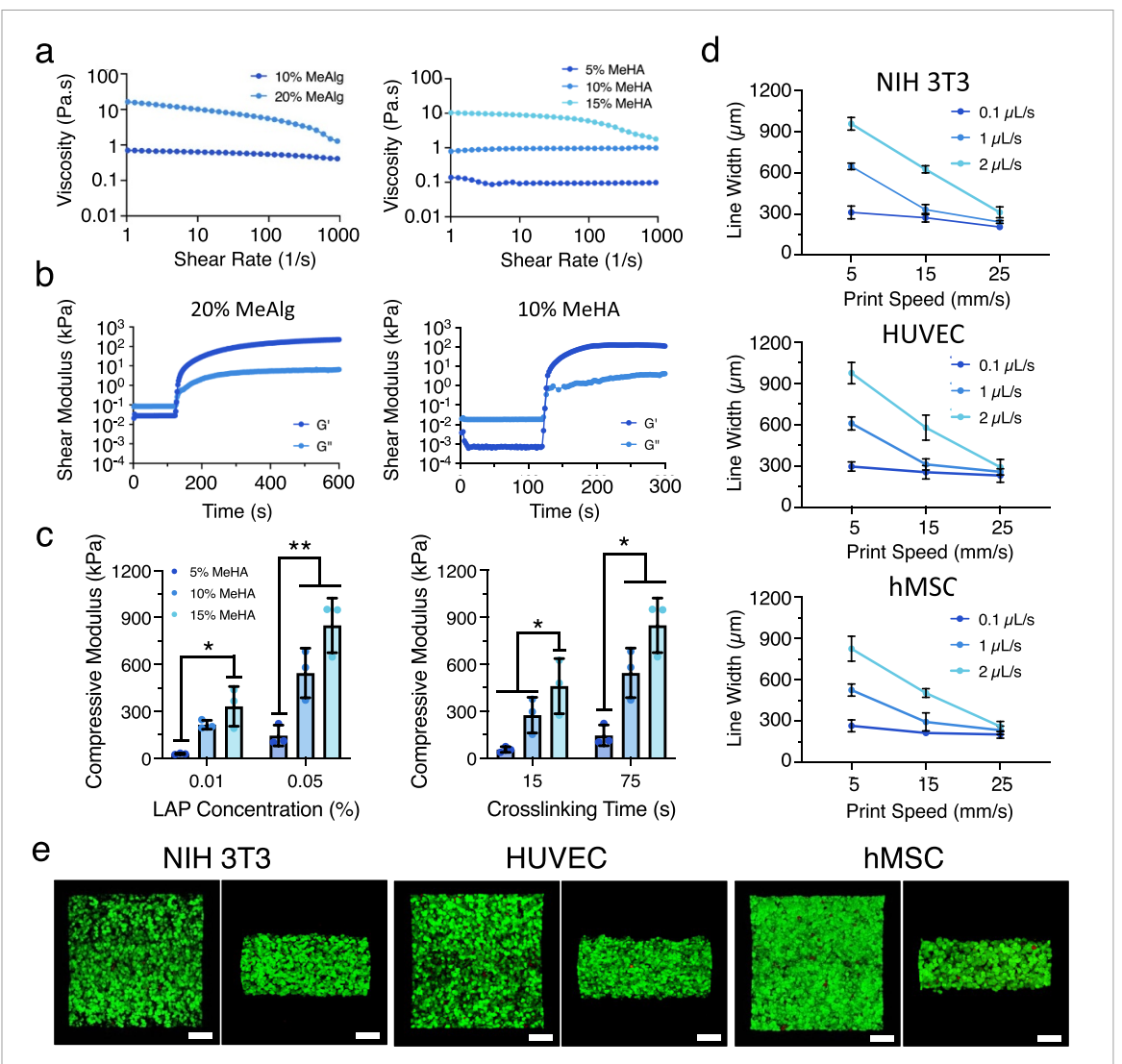


**Figure 3.** Characterization of the hydrogel and cell-only inks. (a) Ink rheology showing MeAlg (10–20 wt/vol%) and MeHA (5–15 wt/vol%) ink viscosity with respect to shear rate. (b) Photorheology of inks (20 wt/vol% MeAlg and 10 wt/vol% MeHA) showing change in shear modulus. The light is turned on at 120 s. (c) Equilibrium Young's modulus values of MeHA hydrogels by varying photoinitiator concentration at a fixed (75 s) light exposure time (left) and for 0.05% LAP at 15 s exposure. Data are presented as mean  $\pm$  SD, \*p < 0.05, \*\*p < 0.01. (d) Line test results showing effect of flow rate and print speed bioprinted NIH3T3, HUVEC, and hMSC strands within 10 wt/vol% MeHA (27 measurements for n = 3). Data are presented as mean  $\pm$  SD. (e) Representative live/dead staining (live in green, and dead in red) images of NIH3T3, HUVEC, and hMSC strands. Scale bars = 100  $\mu$ m.

point (defined at G' = G'') and equilibrium crosslinking time (on set of G'plateau) were  $\sim$ 15 s and  $\sim$ 180 s for MeAlg, and  $\sim$ 5 s and  $\sim$ 75 s for MeHA (figure 3(b)), which remained constant with polymer concentration (figure S1, supporting information). The partial crosslinking time for printed support layer was set to the gel point to ensure mechanical support for bioprinted structures within the support layer. The equilibrium Young's modulus (E) of the MeHA hydrogels was adjusted ( $\sim$ 34–800 kPa) by controlling the light exposure time and photoinitiator concentration for each formulation without altering the viscosity of the inks (figure 3(c)). The adjusted E range is suitable for musculoskeletal tissue engineering including osteochondral tissue interface, which is the focus of this study. However, E can be lowered to Pa range by decreasing the methacrylation of the

polymers independent of polymer concentration or using much lower polymer concentrations including a pre-crosslinking step [46] or a sacrificial thickening agent [47].

To investigate the effect of ink viscosity on print precision, we printed MeHA inks (5, 10, and 15 wt%) within MeAlg support layer (10 or 20 wt%) by varying the print speed (5–25 mm s $^{-1}$ ) and pressure (100–300 kPa). To assess print precision, we tracked printed strut width and circularity (cross-sectional aspect ratio (AR)). MeHA (10 wt%) struts, as low as 63  $\pm$  10  $\mu$ m in width with AR of 1.2  $\pm$  0.1, were printed within MeAlg (20 wt%) for the lowest print pressure and the highest print speed. High print pressures (200–300 kPa) at a low speed (5 mm s $^{-1}$ ) led to spreading of the MeHA struts indicated by larger strut width (300–400  $\mu$ m) and higher AR ( $\sim$ 2.2)

(figures S2 and S3, supporting information). This was more pronounced with decreasing MeHA viscosity (figures S4–S6, supporting information). Increasing MeAlg support layer viscosity led to smaller diameter MeHA struts without affecting the strut circularity for constant print pressure and speed (figure S7, supporting information).

Next, we investigated the effect of MeHA hydrogel support layer viscosity on dense cell bioprinting. First, we bioprinted cell-only strands within 10% MeHA support matrix using a 260  $\mu$ m diameter print nozzle while varying cell aggregate ink flow rate  $(0.1-2 \mu l s^{-1})$  and print speed  $(5-25 \text{ mm s}^{-1})$ . Line width for strands ranged from 206  $\pm$  16–  $956 \pm 46 \ \mu m$  (for NIH3T3s),  $231 \pm 49$ – $975 \pm 77 \ \mu m$ (for HUVECs), and 203  $\pm$  27–827  $\pm$  90  $\mu m$  (for hMSCs), such that line width decreased with decreasing flow rate and increasing print speed (figure 3(d)). High cell viability ( $\sim$ 96%–99%) was observed for strands independent of strand line width (figure 3(e), figures S8-S12, supporting information). Using a smaller size nozzle led to finer strands without compromising cell viability, such that for NIH3T3 aggregates, line width was reduced to 136  $\pm$  14  $\mu$ m and 91  $\pm$  16 for 210 and 160  $\mu$ m nozzle diameter, respectively (figure S13, supporting information). Changing the viscosity of the MeHA support layer (from 0.1 to 10 Pa.s) did not significantly affect the bioprinted hMSC strand line width and cell viability (figure S14, supporting information). Since cell aggregate bioinks used in this study were free of a hydrogel carrier, the time bioinks remained in the print syringe before printing affected cell viability (figure S15, supplementary information). In this study, bioprinting of cell aggregates were completed within 1 h to ensure high cell viability (≥90% for hMSCs and NIH3T3s, and  $\geq 80\%$  for HUVECs) pre-printing.

# 2.3. Effect of support matrix on stem cell behavior during long-term *in vitro* culture

After confirming high cell viability post-printing, we investigated the effect of functional support matrix on cell behavior up to 28 d in vitro. We used MeHA (10%) with (w/) or without (w/o) RGD peptide, which allowed us to study the effect of conjugated RGD-containing cell adhesive oligopeptide on hMSC viability and morphology. The hMSCs showed high cell viability ~96% at day 1 which dropped slightly to  $\sim$ 86% at day 4 and remained constant up to 28 d (figures 4(a) and (b)). Although presence of RGD peptide did not affect cell viability, it led to a significantly higher cell AR and area beginning at day 14 and 21, respectively (figure 4(c)). For RGD conjugated support, AR increased with culture time reaching to 1.9  $\pm$  0.7 at day 14, 3.6  $\pm$  1.9 at day 21 and  $7.1 \pm 2.8$  at day 28 whereas for without RGD support AR was 1.4  $\pm$  0.4, 2.5  $\pm$  0.9 and 2.4  $\pm$  0.9 at day 14, 21 and 28, respectively. This significant

increase in AR could be due to confinement effect as cell strands were trapped within the print line space. Cell confinement has been utilized commonly to align cells leading to high AR [48-54]. Similarly, significant increase in cell area (spreading) was observed at day 21 (267  $\pm$  146  $\mu$ m<sup>2</sup>) and 28 (877  $\pm$  388  $\mu$ m<sup>2</sup>) for MeHA with RGD as compared to without RGD  $(185 \pm 72 \text{ and } 233 \pm 70 \ \mu\text{m}^2 \text{ at day } 21 \text{ and } 28,$ respectively) (figure 4(d)). The increase in cell area and AR were less pronounced when the strands were cultured directly in OM for 28 d (figures S16 and S17, supplementary information), which is expected as stem cells are known to reduce certain functions including proliferation and spreading during differentiation process [44, 55]. These results confirm that cell-adhesive matrix cues, such as integrin binding RGD, directly affects cell morphology, which is known to play a significant role in stem cell differentiation [55–57].

To complement our post-printing viability studies, we also performed *in vitro* culture up to 7 d for NIH3T3 and HUVEC strands embedded within MeHA support. For NIH3T3s, cell viability was  $\sim$ 95%–97% at day 1 and remained constant with culture time whereas for HUVECs, cell viability gradually decreased from  $\sim$ 92% at day 1 to  $\sim$ 50% at day 7 (figures S18 and S19, supplementary information), which was consistent with literature [31]. Like hMSCs, the presence of RGD did not affect cell viability, and no visual differences in cell morphology were observed within 7 d.

# 2.4. Osteogenic differentiation of dense hMSC strands within functional MeHA support

To study osteogenic differentiation of hMSCs, 3D bioprinted dense cell strands within MeHA hydrogel (w/ RGD) were cultured in OM for 14 d. Osteogenic differentiation of hMSCs were confirmed by up regulation of alkaline phosphatase (ALP) activity and calcium deposition (characterized by alizarin red staining (ARS)). Calcium deposition was 2.7-fold higher for day 14 as compared to day 7, and no calcium deposition was observed at day 1 in OM, or at day 14 in GM (figures 5(a) and (b)). ALP activity increased 3.0-fold at day 7 and 7.8-fold at day 14 as compared to day 1. At day 14, ALP activity was 2.5-fold higher in OM as compared to GM (figure 5(b)). Cells showed positive osteocalcin (OC) immunostaining in OM whereas no staining was observed in GM at day 14 (figure 5(c)).

Cell-matrix interactions have long been used to control stem cell morphology [58], and stem cell morphology is considered as an indicator for stem cell fate decision [59]. Spread cell morphology achieved with the presence of integrin-binding leads to activation of mechanotransduction signals involved in osteogenesis, such as Rho kinase and focal adhesion kinase, to enhance osteogenesis [57, 60, 61].

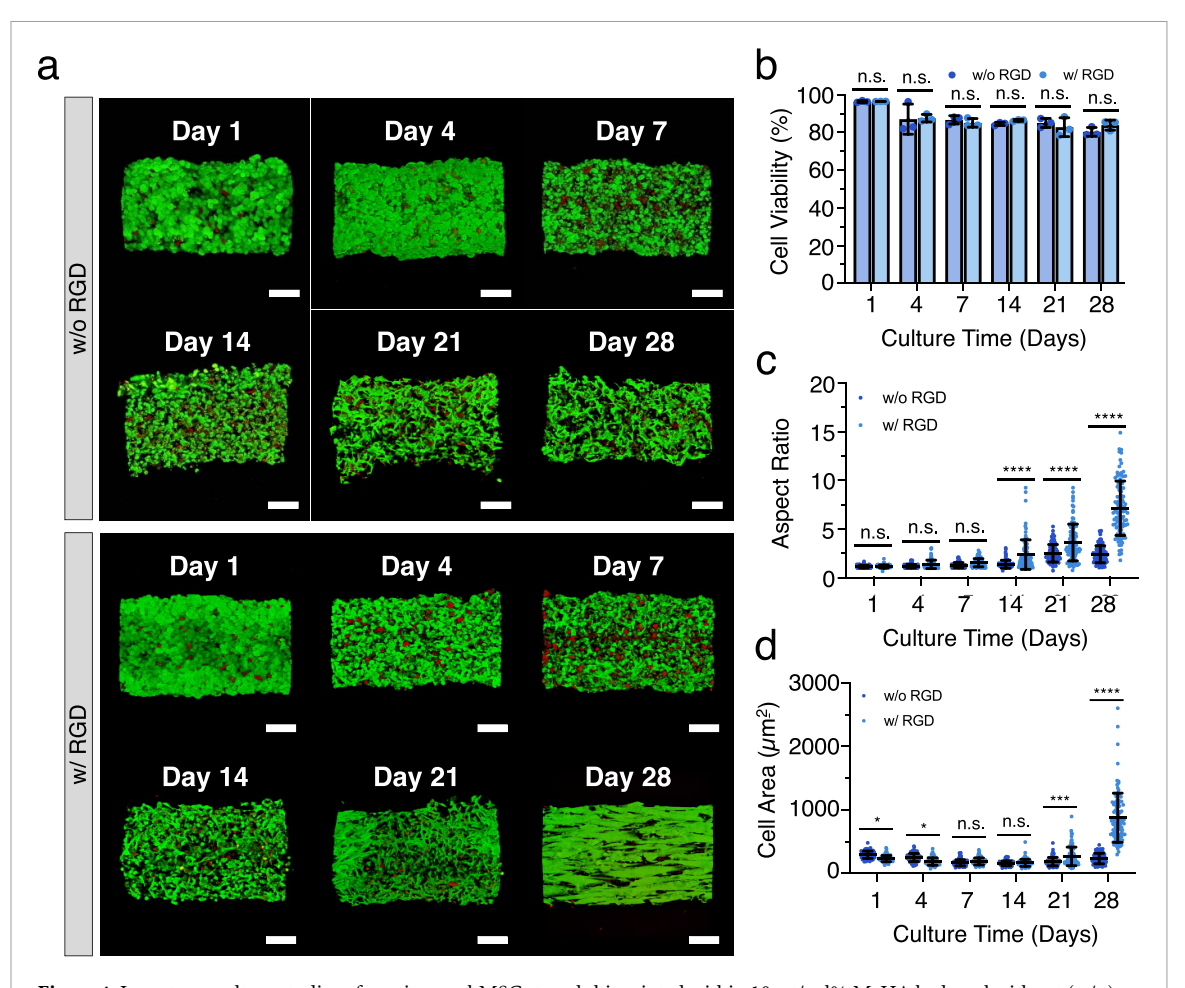


**Figure 4.** Long term culture studies of continuous hMSC strands bioprinted within 10 wt/vol% MeHA hydrogel without (w/o) or with (w/) RGD functionalization. (a) Representative confocal images of hMSCs stained with live/dead staining (live in green, and dead in red). Scale bars =  $100 \, \mu \text{m}$ . (b)–(d) Overall cell viability (b), cell aspect ratio (c), and cell area (d) for hMSCs during culture up to 28 d in growth media. For (b), data are presented as mean  $\pm$  SD for n=3, n.s.: not significant. For (c) and (d), data represent 100 measurements for n=4, \*p<0.05, \*\*\*\*p=0.0006, \*\*\*\*\*p<0.0001.

These observations are based on 2D culture on hydrogels or cell-laden 3D hydrogels and have not yet been explored for bioprinted dense cellular structures embedded within 3D hydrogels. To assess the influence of cell morphology on osteogenic differentiation of dense hMSC strands, strands within MeHA (w/ or w/o RGD) were first cultured in GM for 28 d followed by switching to OM for 14 d. The initial culture in GM ensured that stem cells reached their equilibrium spreading before osteogenic induction. We observed 1.5-fold increase in calcium deposition and 1.3-fold increase in ALP activity (figures 5(d) and (e)) for MeHA with RGD. This finding indicates that support matrix functionalization with integrin binding cell adhesive cues dictate hMSC morphology, and hence, enhance osteogenic differentiation of dense cellular structures.

# 2.5. 3D bioprinting hMSC aggregates within hydrogels with spatiotemporal heterogeneity to modulate stem cell osteogenesis

3D hydrogel systems with spatially and temporally controlled ECM-mimetic heterogeneity are crucial

to promote spatial remodeling of hydrogels as well as stem cell differentiation to create complex tissue interfaces. Spatiotemporal control of 3D hydrogel heterogeneity has been limited to a few techniques which usually rely on complex chemistry and are not suitable for dense cell bioprinting [62]. Here, we demonstrated the control of matrix heterogeneity horizontally (within each layer) and/or vertically (layer-by-layer) to create patterned support hydrogels by simply using different inks during printing of the support layer. The patterned viscous support matrix did not mix with each other, and cell aggregates were easily bioprinted within the patterned viscous support (figures 6(a) and (b)). Here, we focused on horizontally patterned biphasic hydrogels to spatially control hMSC osteogenesis, which is the first step towards regenerating the osteochondral tissue. First, we investigated the effect of MeHA polymer concentration in the presence of RGD (1 mM). We bioprinted hMSC aggregates within three sets of biphasic MeHA (w/ RGD) hydrogels with varying polymer concentration (5%-15%), including 5/10, 5/15 and 10/15 biphasic hydrogels. When cell aggregate bioink

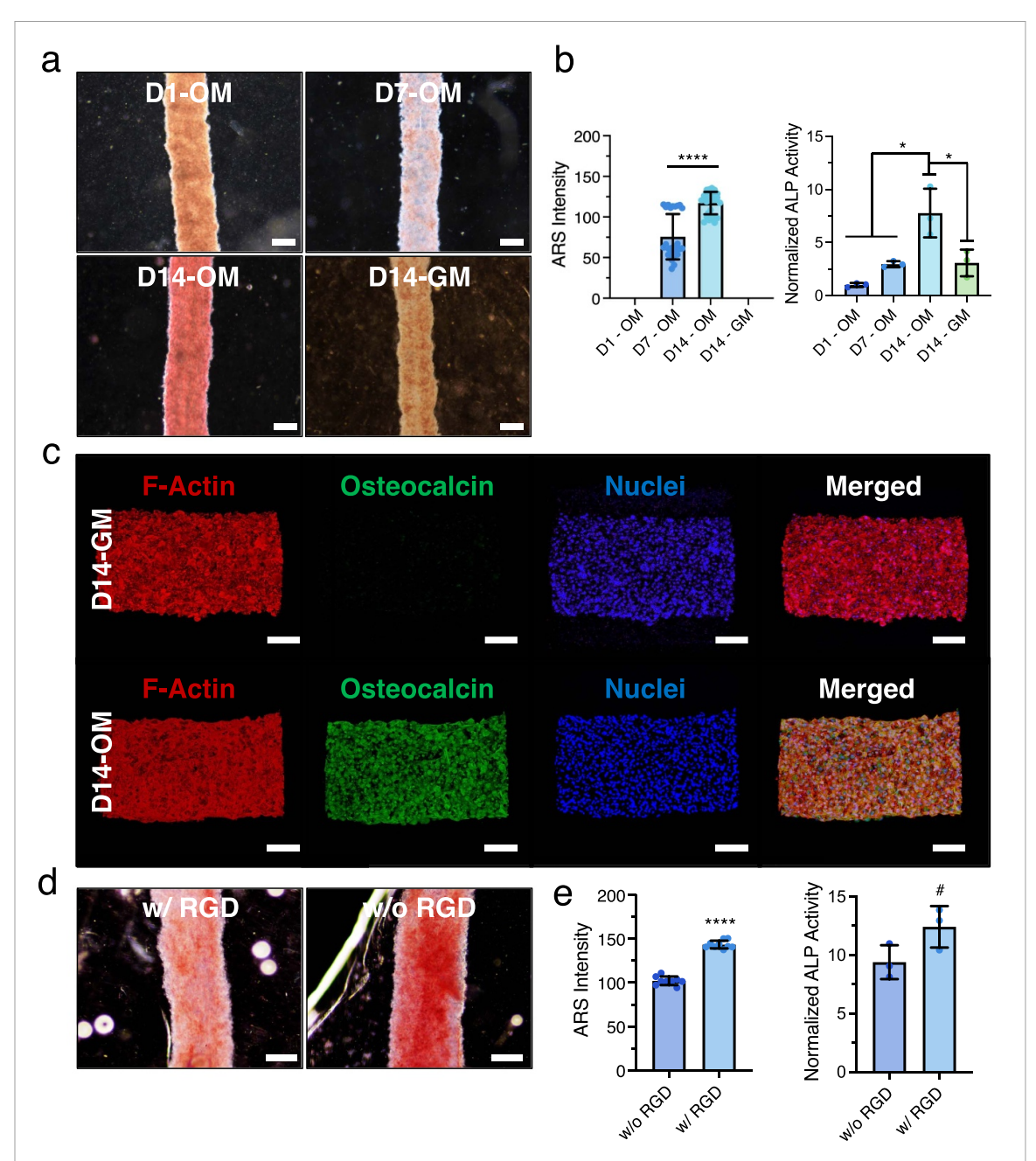
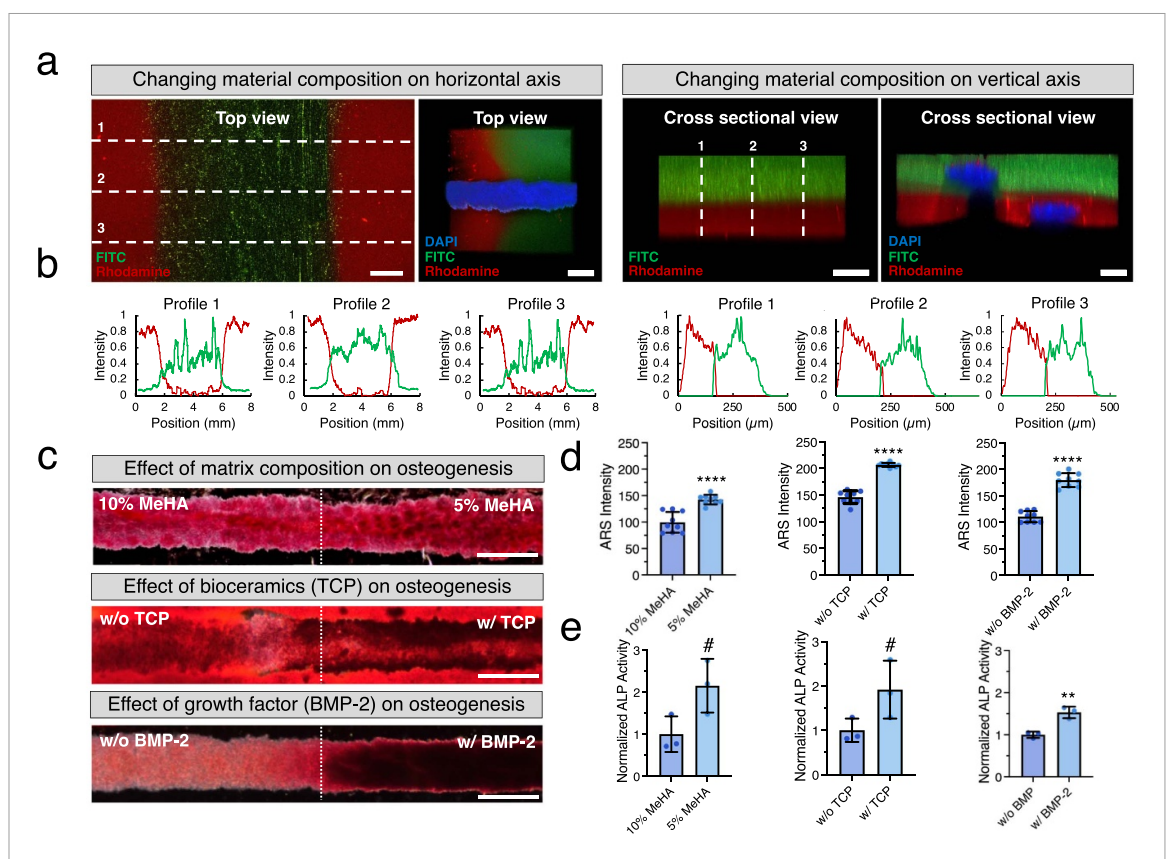


Figure 5. Osteogenic differentiation of continuous hMSC strands bioprinted within 10 wt/vol% MeHA hydrogels. (a) Representative optical images showing calcium deposition (alizarin red staining (ARS) in red) at day 1, 7 and 14 for culture in osteogenic induction media (OM), and at day 14 for growth media (GM). Scale bars = 200  $\mu$ m. (b) ARS intensity (left) and alkaline phosphatase (ALP) activity for culture in OM (days 1, 7 and 14) and GM (day 14). (n=3 independent samples) and ARS intensity (n=9 images from three different samples). Data are presented as mean  $\pm$  SD for n=3 (for ARS, 9 different measurements are done at random locations), \*p<0.05, \*\*\*\*p<0.0001. (c) Representative confocal images of hMSC strands stained for F-actin (red) and nuclei (blue) and immunostained for osteocalcin (green) after 14 d of culture in GM or OM. Scale bars = 100  $\mu$ m. (d) Representative optical images showing calcium deposition in the presence (w/o) or absence (w/o) of RGD moiety for constructs first cultured 28 d in GM followed by 14 d in OM. Scale bars = 200  $\mu$ m. (e) Quantification of osteogenesis for samples in (d) showing ARS intensity and ALP activity. Data are presented as mean  $\pm$  SD for n=3 (for ARS, 9 different measurements are done at random locations), #p=0.0843, \*\*\*\*\*p<0.0001.

was printed within horizontally patterned support layer, the motion of the print needle led to dragging of the matrix material at the interface in the direction of the printing line. The penetration length (PL) of the dragged material was determined by the print speed (5–25 mm s<sup>-1</sup>) and volumetric flow rate of the ink (0.1–2  $\mu$ l s<sup>-1</sup>), such that reducing the print speed and ink flow rate led to smaller PL (figure S20,

supplementary information). The dragging was eliminated when the lowest flow rate (0.1  $\mu$ l s<sup>-1</sup>) and the print speed (5 mm s<sup>-1</sup>) were used. Cell strand line width was uniform across the interface and remained constant around ~400  $\mu$ m for each set (figure S21, supplementary information). After 14 d of culture in GM, cell viability did not change spatially, whereas cell AR and cell area were significantly higher for 5%



**Figure 6.** Controlling support matrix heterogeneity spatiotemporally to control stem cell osteogenesis. (a) Confocal images showing spatial control of hydrogel composition horizontally (right) or vertically (left) (Support I in green: MeHA with FITC beads, support II in red: MeHA with methacrylated rhodamine) for dense cell bioprinting (NIH3T3 strands stained for DAPI, blue). Scale bars =  $200~\mu\text{m}$ . (b) Color intensity profiles showing distinct regions corresponding to dotted lines in (a). (c) Optical images showing representative interface regions of bioprinted hMSC strands stained for calcium deposition after 14 d of culture in OM within biphasic MeHA hydrogel support. Biphasic MeHA includes 10/5~mt/vol% MeHA (top), with or without tricalcium (TCP) particles (middle), and with and without BMP-2 conjugated methacrylated heparin (MeHep). Scale bars =  $200~\mu\text{m}$ . (d) Alizarin red staining intensity for biphasic hydrogels corresponding to (c). (e) ALP activity data corresponding to (c). For (c) and (d), data are presented as mean  $\pm$  SD for n=3 (for ARS, 9 different measurements are done at random locations), #p<0.10, \*\*p=0.0042, \*\*\*\*p<0.0001.

MeHA (AR =  $2.7 \pm 1.0$  and area =  $463 \pm 202 \ \mu m^2$ ) region as compared to 10% (AR =  $1.6 \pm 0.4$  and area =  $219 \pm 60 \ \mu m^2$ ) or 15% (AR =  $1.4 \pm 0.5$  and area =  $237 \pm 75 \ \mu m^2$ ) MeHA region (figure S22, supplementary information). For differentiation studies, we selected the 5/10 biphasic MeHA support as the difference in cell AR and area were not significant between 10 and 15% MeHA regions. After 14 d in OM, ALP activity and calcium deposition was 2.2-fold and  $\sim$ 2.0-fold larger for 5% region as compared 10% region (figures 6(c)–(e)). These findings were due to higher cell AR and area in 5% region and aligned with our results above for monophasic hydrogel supports.

Bioactive cues play important role in influencing stem cell behavior, and in addition to physical cues, chemical signals alone have been shown to direct stem cell differentiation [63–65]. This requires either continuous or temporal exposure of the stem cells to a chemical signal. To show the versatility of our approach, we designed two sets of biphasic supports each composed of 10% MeHA without and with a chemical signal to enhance osteogenesis. In

the first set, we developed a bioceramic composite ink by incorporating tricalcium phosphate (TCP) nanoparticles (<200 nm, 1 w/v%) into 10% MeHA ink. Calcium phosphate (CP) moieties have been commonly incorporated into engineered microenvironments to promote osteogenic differentiation of hMSCs [66–69], yet this is difficult to apply for dense cell bioprinting platforms. Incorporation of TCP particles slightly increased the ink viscosity but did not alter the crosslinking kinetics, the *E* of the hydrogel, or bioprinted cell strand line width (figure S23, supplementary information). When hMSC strands were cultured within biphasic support (composed of 10% MeHA w/ or w/o TCP) for 14 d in OM, strands within the composite support region showed higher ALP activity ( $\sim$ 1.9-fold increase) and calcium deposition (~1.6-fold increase in ARS intensity) as compared to neat hydrogel region (figures 6(c)–(e)). These findings indicate that TCP-laden support matrix significantly enhances stem cell osteogenesis.

In the second set, we focused on controlled delivery of bone morphogenic protein 2 (BMP-2) as it has been widely used to enhance stem cell

osteogenesis. To achieve controlled release, we used heparin macromer, which is known to sequester growth factors including BMP-2 [70]. Methacrylated heparin (MeHep) has been previously used for temporal delivery of BMP-2 within cell-laden 3D hydrogels for bone tissue engineering [71–73]. Here, we synthesized MeHep (~18% methacrylation, figure S24, supplementary information) to formulate a MeHA/MeHep blend ink containing 10% MeHA and 1% MeHep conjugated with BMP-2 (100 ng ml $^{-1}$ ). The viscosity and the crosslinking kinetics (gel point and equilibrium crosslinking time) of the inks, the E of the hydrogels, and bioprinted cell strand line width remained constant for blends as compared to neat MeHA (figure \$25, supplementary information). The hMSC strands embedded within the region conjugated with BMP-2 showed significantly higher ALP activity (~1.5-fold) and calcium deposition (~1.9fold) (figures 6(c)–(e)). When MeHep was replaced with Hep (conjugated with BMP-2, 100 ng ml<sup>-1</sup>), no significant differences in ALP activity and calcium deposition were observed between MeHA and MeHA/Hep(w/BMP-2) regions (figure S26, supplementary information). These results show that spatiotemporal release of BMP-2 leads to local enhancement of stem cell osteogenesis. Although the BMP-2 release was not measured, the evidence of cellular activity indicates that crosslinking Hep macromer to MeHA support matrix (in the form of MeHep) provides sustained release of BMP-2 as compared to free Hep macromer blended in MeHA support which is known to result in immediate release of heparin/BMP-2 conjugate [74]. When monophasic MeHA constructs were used as a control, dosing of OM media with BMP-2 during each media change led to an increase in ALP activity (~1.2-fold) and calcium deposition ( $\sim$ 1.5-fold) as compared to regular OM (figure S27, supplementary information). These observations clearly show the potential of the approach to fabricate continuous dense cellular structures within hydrogel supports where cell behavior can be controlled locally by spatially modulating the matrix functionality through physical and biochemical cues.

### 3. Conclusion

Embedded dense cell bioprinting is an emerging technology for biofabrication of dense tissue constructs providing developmentally relevant cell-cell interactions. However, the support hydrogel matrices are usually regarded as temporary support or only provide uniform properties (when designed for prolonged culture) rather than providing spatially controlled ECM mimetic cues for local modulation of cellular function. This is particularly important to create tissue interfaces in which cellular and ECM composition vary locally. To address this challenge, we report a bioprinting approach enabling to deposit

dense cellular structures within a wide range of photocurable hydrogels as support matrices. We demonstrate fabrication of dense multi-cellular structures using hMSC, NIH3T3, and HUVEC aggregates. The hMSC strands embedded within MeHA hydrogels show significantly increased cellular spreading and AR when MeHA support is functionalized with cell adhesive RGD peptides leading to enhanced osteogenesis. By using multi-material printing, we demonstrate fabrication of biphasic MeHA support hydrogels in which polymer concentration or bone promoting cues such as TCP particles and BMP-2 are spatially controlled. When polymer concentration is varied, hMSC strands show significantly higher cellular spreading and AR in low concentration (5%) region as compared to higher concentration (10% or 15%) regions, and these changes lead to a significantly higher upregulation of osteogenesis locally for low concentration region. When polymer concentration is kept constant, biphasic scaffolds with TCP containing regions significantly enhance stem cell osteogenesis. Similarly, spatial release of BMP-2 is shown to enhance stem cell osteogenesis locally. Overall, our study demonstrates fabrication of dense cellular constructs within cell instructive hydrogels and local modulation of stem cell function by spatial control of cell instructive cues. This approach is a step towards creating highly heterogenous tissue interfaces such as osteochondral tissue with much needed cellular and matrix complexity.

# 4. Experimental section

## 4.1. Ink formulation

MeAlg, MeHA, and MeHep were synthesized as previously described [55, 75] using alginic acid sodium salt (Sigma-Aldrich), sodium HA (60 kDa, LifeCore Biomedical), and heparin sodium salt (IU  $\geq$  100 mg<sup>-1</sup>, Thermo Fisher), respectively. Each polymer was dissolved in deionized (DI) water and reacted with methacrylic anhydride (Sigma-Aldrich) at 1 °C-4 °C for 8 h while pH was kept at 8-9 by dropwise addition of 4 M sodium hydroxide (Sigma-Aldrich) solution. After the solution was kept overnight at 4 °C, the reaction was continued for 4 h at 1 °C-4 °C by dropwise addition of MA while maintaining the pH between 8-9. The solution was then dialyzed for 5 d, frozen at—80 °C, and lyophilized. The degree of modification was determined by <sup>1</sup>H NMR (Bruker, figure S28, supporting information). Hydrogel inks were formulated as MeHA (5, 10, and 15 wt/vol%) or MeAlg (10 and 20 wt/vol%) dissolved in Dulbecco's phosphate buffered saline (DPBS, Sigma-Aldrich) in presence of a photoinitiator (0.05 wt/vol%), lithium phenyl-2,4,6-trimethyl benzoylphosphinate (LAP, 405-410 nm, Sigma-Aldrich). When needed, RGD peptide (50 mg ml<sup>-1</sup>, GRGDSPC, GenScript) was added (10  $\mu$ l ml<sup>-1</sup> of ink formulation) and incubated at room temperature (RT) at least for 30 min, such that the final concentration of RGD was 1 mM [55, 75]. For cell-laden inks, the formulation was mixed with 100  $\mu$ l of cell suspension (1 × 10<sup>7</sup> cells ml<sup>-1</sup>). For TCP containing composite MeHA inks, MeHA (10 w/v%) was dissolved in TCP (<200 nm, Sigma-Aldrich) suspension in DPBS (1 wt/vol%). BMP-2 containing MeHA inks were formulated as 10 wt/vol% MeHA, 1 wt/vol% MeHep (or Hep) conjugated with 1  $\mu$ g ml<sup>-1</sup> BMP-2 (Genscript) (supplementary methods, supporting information).

Cell aggregate inks were prepared from three different cell types (NIH3T3s, HUVECs, and hMSCs) obtained from Lonza. Each cell type was expanded following the suggested culture protocols from the supplier (supplementary methods, supporting information). Cells were collected into 50 ml centrifuge tubes with fresh growth media and centrifuged to obtain cell pellets. Cell pellets were combined into a 50 ml centrifuge tube after filtration through 40  $\mu$ m cell strainer to remove cell clumps to avoid clogging during printing. After final centrifugation, cell aggregate ( $\geq 50 \times 10^6$  cells) was sucked into a 3 ml syringe and immediately used as a bioink.

#### 4.2. Rheological characterization

Kinexus Prime Ultra+ rheometer (Netzsch) was used for rheological characterization. Tests were performed using a 20 mm flat upper plate geometry and 0.75 mm gap size. The shear viscosity was measured for shear rates between 0.01-1000 s<sup>-1</sup>. For photocrosslinking studies, a Kinexus light curing system (Netzsch) equipped with a light source (Omnicure S2000, 365 nm, 40 mW cm $^{-2}$ ) was used. Time sweep tests were performed (at 1 Hz and 1% strain) while monitoring the change in elastic (G') and viscous modulus (G''). The light was turned on after 2 min of equilibrium run. The light intensity was adjusted to compensate for the difference in the wavelength for the printer (405 nm) according to the molar absorptivity spectrum of the photoinitiator (LAP) [76]. Frequency sweep (0.1–100 Hz) tests were performed at 1% strain on MeHA hydrogels that were equilibrated overnight in PBS. Compression tests were also performed on equilibrated hydrogels (1 mm thick and 25 mm in diameter) by applying a normal force starting from 0.05 N up to 10 N at a rate of 0.1 mm s<sup>-1</sup>. Young's modulus (E) was calculated using the linear portion of the stress-strain curve within 5% strain.

### 4.3. Bioprinting and cell culture

Bio X<sup>TM</sup> 3D bioprinter (CellInk) was used for bioprinting. Inks were printed from 3 ml syringes. Pneumatic printheads (CellInk) were used for hydrogel inks whereas cell-only bioinks were printed using a syringe pump printhead (CellInk) for more precise extrusion. Printing was done on a microscope slide for easy handling. Cell-laden samples were placed

in 6-well plates immediately after printing, covered with growth media (respective to each cell type), and placed in an incubator. Media was changed every three days for samples containing NIH3T3s and hMSCs, and every two days for HUVECs. For multicellular prints, a mixed growth media (equal parts) was used.

### 4.4. Printability and cell viability studies

Printability studies were done by printing MeHA ink formulations in the form 10 mm long struts within MeAlg supports (15 mm × 15 mm) at different extrusion pressures (100-300 kPa) and print speeds  $(5-25 \text{ mm s}^{-1})$ . To determine circularity, confocal images were obtained from MeHA struts containing FITC labeled-fluorescent beads (Fluoresbrite® YG Microspheres, 0.20  $\mu$ m, Polysciensec), and AR (width/height) was measured using cross-sectional images using ImageJ (NIH). For printability of cellonly bioinks, cell aggregates (NIH3T3, HUVECs, or hMSCs) were printed as 10 mm long continuous struts within MeHA hydrogels (15 mm × 15 mm) at varying flow rates (0.1–2  $\mu$ l s<sup>-1</sup>) and print speeds  $(5-25 \text{ mm s}^{-1})$ . Optical images were used for line width measurements using ImageJ (NIH). Cell viability studies were done using a Live/Dead TM staining kit (Thermo Fisher Scientific). Samples were incubated in calcein AM (Live, 0.5  $\mu$ l per ml of DPBS) and ethidium homodimer (Dead, 2  $\mu$ l per ml of DPBS) for 30 min at RT. Samples were then washed with DPBS (3x) and immediately imaged under confocal microscope to obtain z-stack images (≥3 images per sample). All fluorescent images were taken using a 2photon confocal microscope (Leica).

#### 4.5. Cell culture and differentiation studies

3D printed constructs were cultured in growth media for each cell type. For hMSCs, minimum essential medium  $\alpha$  supplemented with 10 vol/vol% fetal bovine serum (FBS) and 1 vol/vol% penicillinstreptomycin (pen-strep) was used. Culture media for NIH3T3s was composed of high glucose Dulbecco's modified Eagle medium, 10 vol/vol% FBS, and 1 vol/vol% pen-strep. For HUVECs, endothelial cell growth medium (EGM-2 BulletKit, Lonza) was used. For differentiation studies, hMSC osteogenic differentiation medium (OM) BulletKit<sup>TM</sup> (Lonza) was used.

To quantify cell spreading, cells were stained with Live/Dead<sup>TM</sup> staining kit and nuclei were stained with DAPI. Z-stack images were obtained using a confocal microscope. Cell area and AR ( $\geqslant$ 100 cells per sample) were calculated using ImageJ. The quantitative data was confirmed using fixed cells stained for F-actin and DAPI. Osteogenic differentiation was characterized by measuring ALP activity and calcium deposition. ALP activity was measured using QuantiChrom<sup>TM</sup> Alkaline Phosphatase Assay Kit (BioAssay Systems). Constructs were pulverized in 400  $\mu$ l lysis buffer (0.25% Triton-X in DI water) and

incubated overnight in 1.5 ml microcentrifuge tubes. Each vial was centrifuged, and the supernatant (50  $\mu$ l) was reacted with p-nitrophenyl phosphate working solution in 96-well plates. Absorbance values were measured at 405 nm using a plate reader (Infinite M200 Pro, Tecan), and were normalized by DNA content, which was quantified by using PicoGreen assay (Quant-iTTM PicoGreenTM dsDNA Assay Kit, Invitrogen). For DNA content, fluorescence intensity values were measured using at 480 nm excitation and 520 nm emission wavelength. Calcium deposition was evaluated using Alizarin Red staining kit (Sigma). Constructs were rinsed with DPBS (2x), fixed in ice-cold 75% ethanol for 2 h, rinsed with DI water (2x), and incubated in Alizarin Red solution overnight. Constructs were washed with DI water and imaged using an optical microscope. Images were converted to 8-bit images and inverted to measure the staining intensity by ImageJ.

### 4.6. Immunofluorescence staining

Printed constructs were washed with DPBS (3x) and fixed with 4% paraformaldehyde in PBS for 25 min. The constructs were then washed with DPBS (3x) and incubated with 0.25% Triton X-100 in PBS for 1 h. They were blocked with 10% donkey serum in PBS containing 0.01% Triton-X for 3 h and then incubated with the primary antibody diluted in blocking solution against osteocalcin (1:200; monoclonal mouse, Invitrogen) for 48 h at 4 °C. After washing with blocking solution, samples were incubated overnight at 4 °C with secondary antibody Alexa Fluor 488 rabbit anti-mouse in blocking solution (1:100, Invitrogen), and/or rhodamine phalloidin (1:400, Invitrogen), and DAPI (1:2000, Sigma). After washing with DPBS, samples were imaged under a confocal microscope.

# 4.7. Printing within biphasic matrix

To visualize patterned hydrogels, support inks were mixed with either FITC-labeled fluorescent beads or methacrylated rhodamine. Color intensity profiles were measured using ImageJ to study pattern uniformity. Two different support ink formulations were printed sequentially to create biphasic (patterned) support layer followed by hMSC aggregate printing within this layer.

## 4.8. Statistical analysis

Data were analyzed using Minitab® statistical software (Minitab, LLC). Unless otherwise specified, data were reported as mean  $\pm$  SD for  $n \ge 3$ . One-way or two-way ANOVA with Tukey's post hoc test was used to make comparisons. Significance determined by p < 0.05 (\*\*\*\*p < 0.0001, \*\*\*p < 0.001, \*\*p < 0.05, #p < 0.10).

# Data availability statements

The data cannot be made publicly available upon publication because they contain commercially sensitive information. The data that support the findings of this study are available upon reasonable request from the authors.

# Acknowledgments

This work was supported by the National Science Foundation CAREER Award (DMR-2044479) and a New Jersey Health Foundation grant.

### **Conflict of interest**

The printing approach described in this study was patented by New Jersey Institute of Technology (US Patent 11 806 444).

#### ORCID iD

Murat Guvendiren https://orcid.org/0000-0002-3475-1051

#### References

- [1] Daly A C, Prendergast M E, Hughes A J and Burdick J A 2021 Bioprinting for the biologist *Cell* 184 18–32
- [2] Sun W et al 2020 The bioprinting roadmap Biofabrication 12 022002
- [3] Moroni L, Burdick J A, Highley C, Lee S J, Morimoto Y, Takeuchi S and Yoo J J 2018 Biofabrication strategies for 3D in vitro models and regenerative medicine *Nat. Rev. Mater.* 3 21–37
- [4] Zhang Y S et al 2017 3D bioprinting for tissue and organ fabrication Ann. Biomed. Eng. 45 148–63
- [5] Xie R, Pal V, Yu Y, Lu X, Gao M, Liang S, Huang M, Peng W and Ozbolat I T 2024 A comprehensive review on 3D tissue models: biofabrication technologies and preclinical applications *Biomaterials* 304 122408
- [6] Lee A, Hudson A R, Shiwarski D J, Tashman J W, Hinton T J, Yerneni S, Bliley J M, Campbell P G and Feinberg A W 2019 3D bioprinting of collagen to rebuild components of the human heart Science 365 482–7
- [7] Mirdamadi E, Tashman J W, Shiwarski D J, Palchesko R N and Feinberg A W 2020 FRESH 3D bioprinting a full-size model of the human heart ACS Biomater. Sci. Eng. 6 6453–9
- [8] Finkel S et al 2023 FRESH<sup>TM</sup> 3D bioprinted cardiac tissue, a bioengineered platform for in vitro pharmacology APL Bioeng. 7 046113
- [9] Bliley J, Tashman J, Stang M, Coffin B, Shiwarski D, Lee A, Hinton T and Feinberg A 2022 FRESH 3D bioprinting a contractile heart tube using human stem cell-derived cardiomyocytes *Biofabrication* 14 024106
- [10] Skylar-Scott M A, Uzel S G M, Nam L L, Ahrens J H, Truby R L, Damaraju S and Lewis J A 2019 Biomanufacturing of organ-specific tissues with high cellular density and embedded vascular channels *Sci. Adv.* 5 eaaw2459
- [11] Bhattacharjee T, Zehnder S M, Rowe K G, Jain S, Nixon R M, Sawyer W G and Angelini T E 2015 Writing in the granular gel medium Sci. Adv. 1 e1500655
- [12] Hinton T J, Jallerat Q, Palchesko R N, Park J H, Grodzicki M S, Shue H-J, Ramadan M H, Hudson A R and

- Feinberg A W 2015 Three-dimensional printing of complex biological structures by freeform reversible embedding of suspended hydrogels *Sci. Adv.* 1 e1500758
- [13] Highley C B, Rodell C B and Burdick J A 2015 Direct 3D printing of shear-thinning hydrogels into self-healing hydrogels Adv. Mater. 27 5075–9
- [14] Highley C B, Song K H, Daly A C and Burdick J A 2019 Jammed microgel inks for 3D printing applications Adv. Sci. 6 1801076
- [15] Zhang Y, Ellison S T, Duraivel S, Morley C D, Taylor C R and Angelini T E 2021 3D printed collagen structures at low concentrations supported by jammed microgels *Bioprinting* 21 e00121
- [16] Duraivel S, Laurent D, Rajon D A, Scheutz G M, Shetty A M, Sumerlin B S, Banks S A, Bova F J and Angelini T E 2023 A silicone-based support material eliminates interfacial instabilities in 3D silicone printing *Science* 379 1248–52
- [17] O'Bryan C S, Bhattacharjee T, Hart S, Kabb C P, Schulze K D, Chilakala I, Sumerlin B S, Sawyer W G and Angelini T E 2017 Self-assembled micro-organogels for 3D printing silicone structures Sci. Adv. 3 e1602800
- [18] Kajtez J et al 2022 Embedded 3D printing in self-healing annealable composites for precise patterning of functionally mature human neural constructs Adv. Sci. 9 2201392
- [19] Lindsay C D, Roth J G, LeSavage B L and Heilshorn S C 2019 Bioprinting of stem cell expansion lattices *Acta Biomater*. 95 225–35
- [20] Song K H, Highley C B, Rouff A and Burdick J A 2018 Complex 3D-printed microchannels within cell-degradable hydrogels Adv. Funct. Mater. 28 1801331
- [21] Choi Y-J et al 2019 A 3D cell printed muscle construct with tissue-derived bioink for the treatment of volumetric muscle loss Biomaterials 206 160–9
- [22] Noor N, Shapira A, Edri R, Gal I, Wertheim L and Dvir T 2019 3D printing of personalized thick and perfusable cardiac patches and hearts Adv. Sci. 6 1900344
- [23] Ayan B, Celik N, Zhang Z, Zhou K, Kim M H, Banerjee D, Wu Y, Costanzo F and Ozbolat I T 2020 Aspiration-assisted freeform bioprinting of pre-fabricated tissue spheroids in a yield-stress gel Commun. Phys. 3 183
- [24] Ayan B, Wu Y, Karuppagounder V, Kamal F and Ozbolat I T 2020 Aspiration-assisted bioprinting of the osteochondral interface Sci. Rep. 10 13148
- [25] Roth J G, Brunel L G, Huang M S, Liu Y, Cai B, Sinha S, Yang F, Paşca S P, Shin S and Heilshorn S C 2023 Spatially controlled construction of assembloids using bioprinting Nat. Commun. 14 4346
- [26] Daly A C, Davidson M D and Burdick J A 2021 3D bioprinting of high cell-density heterogeneous tissue models through spheroid fusion within self-healing hydrogels Nat. Commun. 12 753
- [27] Kim M H, Banerjee D, Celik N and Ozbolat I T 2022 Aspiration-assisted freeform bioprinting of mesenchymal stem cell spheroids within alginate microgels *Biofabrication* 14 024103
- [28] Mecit Altan A et al 2023 Nested biofabrication: matryoshka-inspired intra-embedded bioprinting bioRxiv http://doi.org/10.1101/2023.09.28.560028
- [29] Banerjee D, Ivanova M M, Celik N, Kim M H, Derman I D, Limgala R P, Ozbolat I T and Goker-Alpan O 2023 Biofabrication of an in-vitro bone model for Gaucher disease *Biofabrication* 15 045023
- [30] Bhattacharjee T et al 2016 Liquid-like solids support cells in 3D ACS Biomater. Sci. Eng. 2 1787–95
- [31] Brassard J A, Nikolaev M, Hübscher T, Hofer M and Lutolf M P 2021 Recapitulating macro-scale tissue self-organization through organoid bioprinting *Nat. Mater.* 20 22–29
- [32] Jeon O, Lee Y B, Jeong H, Lee S J, Wells D and Alsberg E 2019 Individual cell-only bioink and photocurable supporting medium for 3D printing and generation of engineered tissues with complex geometries *Mater. Horiz.* 6 1625–31

- [33] Ding A, Lee S J, Tang R, Gasvoda K L, He F and Alsberg E 2022 4D cell-condensate bioprinting Small 18 2202196
- [34] Hull S M, Brunel L G and Heilshorn S C 2022 3D bioprinting of cell-laden hydrogels for improved biological functionality Adv. Mater. 34 2103691
- [35] Hull S M, Lou J, Lindsay C D, Navarro R S, Cai B, Brunel L G, Westerfield A D, Xia Y and Heilshorn S C 2023 3D bioprinting of dynamic hydrogel bioinks enabled by small molecule modulators Sci. Adv. 9 eade7880
- [36] Caliari S R and Burdick J A 2016 A practical guide to hydrogels for cell culture Nat. Methods 13 405–14
- [37] Chimene D, Lennox K K, Kaunas R R and Gaharwar A K 2016 Advanced bioinks for 3D printing: a materials science perspective Ann. Biomed. Eng. 44 2090–102
- [38] Chimene D, Kaunas R and Gaharwar A K 2020 Hydrogel bioink reinforcement for additive manufacturing: a focused review of emerging strategies Adv. Mater. 32 1902026
- [39] Zhang Y S and Khademhosseini A 2017 Advances in engineering hydrogels *Science* **356** eaaf3627
- [40] Gungor-Ozkerim P S, Inci I, Zhang Y S, Khademhosseini A and Dokmeci M R 2018 Bioinks for 3D bioprinting: an overview *Biomater. Sci.* 6 915–46
- [41] Hull S M, Lindsay C D, Brunel L G, Shiwarski D J, Tashman J W, Roth J G, Myung D, Feinberg A W and Heilshorn S C 2021 3D bioprinting using UNIversal orthogonal network (UNION) bioinks Adv. Funct. Mater. 31 2007983
- [42] Reilly G C and Engler A J 2010 Intrinsic extracellular matrix properties regulate stem cell differentiation J. Biomech. 43 55–62
- [43] Discher D E, Janmey P and Wang Y-L 2005 Tissue cells feel and respond to the stiffness of their substrate *Science* 310 1139–43
- [44] Huebsch N, Arany P R, Mao A S, Shvartsman D, Ali O A, Bencherif S A, Rivera-Feliciano J and Mooney D J 2010 Harnessing traction-mediated manipulation of the cell/matrix interface to control stem-cell fate *Nat. Mater.* 9 518–26
- [45] Ji S, Abaci A, Morrison T, Gramlich W M and Guvendiren M 2020 Novel bioinks from UV-responsive norbornene-functionalized carboxymethyl cellulose macromers *Bioprinting* 18 e00083
- [46] Rutz A L, Hyland K E, Jakus A E, Burghardt W R and Shah R N 2015 A multimaterial bioink method for 3D printing tunable, cell-compatible hydrogels Adv. Mater. 27 1607–14
- [47] Riffe M B, Davidson M D, Seymour G, Dhand A P, Cooke M E, Zlotnick H M, McLeod R R and Burdick J A 2024 Multi-material volumetric additive manufacturing of hydrogels using gelatin as a sacrificial network and 3D suspension bath Adv. Mater. 2309026
- [48] Tang Q Y, Tong W Y, Shi J, Shi P, Lam Y W and Pang S W 2014 Influence of engineered surface on cell directionality and motility *Biofabrication* 6 015011
- [49] Loesberg W A, te Riet J, van Delft F C M J M, Schön P, Figdor C G, Speller S, Vanloon J, Walboomers X and Jansen J 2007 The threshold at which substrate nanogroove dimensions may influence fibroblast alignment and adhesion Biomaterials 28 3944–51
- [50] Wong L, Pegan J D, Gabela-Zuniga B, Khine M and McCloskey K E 2017 Leaf-inspired microcontact printing vascular patterns *Biofabrication* 9 021001
- [51] Guvendiren M and Burdick J A 2010 The control of stem cell morphology and differentiation by hydrogel surface wrinkles *Biomaterials* 31 6511–8
- [52] House A, Cornick J, Butt Q and Guvendiren M 2023 Elastomeric platform with surface wrinkling patterns to control cardiac cell alignment J. Biomed. Mater. Res. A 111 1228–42
- [53] Alioglu M A, Singh Y P, Nagamine M, Rizvi S H A, Pal V, Gerhard E M, Saini S, Kim M H and Ozbolat I T 2023 3D embedded printing of microfluidic devices using a functional silicone composite support bath Addit. Manuf. 70 103566

- [54] Aubin H, Nichol J W, Hutson C B, Bae H, Sieminski A L, Cropek D M, Akhyari P and Khademhosseini A 2010 Directed 3D cell alignment and elongation in microengineered hydrogels *Biomaterials* 31 6941–51
- [55] Khetan S, Guvendiren M, Legant W R, Cohen D M, Chen C S and Burdick J A 2013 Degradation-mediated cellular traction directs stem cell fate in covalently crosslinked three-dimensional hydrogels Nat. Mater. 12 458–65
- [56] Guilak F, Cohen D M, Estes B T, Gimble J M, Liedtke W and Chen C S 2009 Control of stem cell fate by physical interactions with the extracellular matrix *Cell Stem Cell* 5 17–26
- [57] McBeath R, Pirone D M, Nelson C M, Bhadriraju K and Chen C S 2004 Cell shape, cytoskeletal tension, and RhoA regulate stem cell lineage commitment *Dev. Cell* 6 483–95
- [58] Kilian K A, Bugarija B, Lahn B T and Mrksich M 2010 Geometric cues for directing the differentiation of mesenchymal stem cells Proc. Natl Acad. Sci. 107 4872–7
- [59] Treiser M D, Yang E H, Gordonov S, Cohen D M, Androulakis I P, Kohn J, Chen C S and Moghe P V 2010 Cytoskeleton-based forecasting of stem cell lineage fates Proc. Natl Acad. Sci. USA 107 610-5
- [60] Shih Y-R V, Tseng K-F, Lai H-Y, Lin C-H and Lee O K 2011 Matrix stiffness regulation of integrin-mediated mechanotransduction during osteogenic differentiation of human mesenchymal stem cells J. Bone Miner. Res. 26 730–8
- [61] Salasznyk R M, Klees R F, Williams W A, Boskey A and Plopper G E 2007 Focal adhesion kinase signaling pathways regulate the osteogenic differentiation of human mesenchymal stem cells Exp. Cell Res. 313 22–37
- [62] Brown T E and Anseth K S 2017 Spatiotemporal hydrogel biomaterials for regenerative medicine *Chem. Soc. Rev.* 46 6532–52
- [63] Putra V D L, Kilian K A and Knothe Tate M L 2023 Biomechanical, biophysical and biochemical modulators of cytoskeletal remodelling and emergent stem cell lineage commitment Commun. Biol. 6 75
- [64] Li J et al 2021 Biophysical and biochemical cues of biomaterials guide mesenchymal stem cell behaviors Front. Cell Develop. Biol. 9 640388
- [65] Ding S, Kingshott P, Thissen H, Pera M and Wang P-Y 2017 Modulation of human mesenchymal and pluripotent stem

- cell behavior using biophysical and biochemical cues: a review *Biotechnol. Bioeng.* 114 260–80
- [66] Bose S, Vahabzadeh S and Bandyopadhyay A 2013 Bone tissue engineering using 3D printing Mater. Today 16 496–504
- [67] Lu J, Yu H and Chen C 2018 Biological properties of calcium phosphate biomaterials for bone repair: a review RSC Adv. 8 2015–33
- [68] Samavedi S, Whittington A R and Goldstein A S 2013 Calcium phosphate ceramics in bone tissue engineering: a review of properties and their influence on cell behavior Acta Biomater. 9 8037–45
- [69] Shih Y-R V et al 2014 Calcium phosphate-bearing matrices induce osteogenic differentiation of stem cells through adenosine signaling Proc. Natl Acad. Sci. 111 990–5
- [70] Martino M M, Briquez P S, Ranga A, Lutolf M P and Hubbell J A 2013 Heparin-binding domain of fibrin(ogen) binds growth factors and promotes tissue repair when incorporated within a synthetic matrix *Proc. Natl Acad. Sci.* 110 4563–8
- [71] Jeon O, Powell C, Solorio L D, Krebs M D and Alsberg E 2011 Affinity-based growth factor delivery using biodegradable, photocrosslinked heparin-alginate hydrogels J. Control. Release 154 258–66
- [72] Jeon O, Lee K and Alsberg E 2018 Spatial micropatterning of growth factors in 3D hydrogels for location-specific regulation of cellular behaviors Small 14 1800579
- [73] Ruppert R, Hoffmann E and Sebald W 1996 Human bone morphogenetic protein 2 contains a heparin-binding site which modifies its biological activity *Eur. J. Biochem.* 237 295–302
- [74] Brown G C J, Lim K S, Farrugia B L, Hooper G J and Woodfield T B F 2017 Covalent incorporation of heparin improves chondrogenesis in photocurable gelatin-methacryloyl hydrogels *Macromol. Biosci.* 17 1700158
- [75] Guvendiren M and Burdick J A 2012 Stiffening hydrogels to probe short- and long-term cellular responses to dynamic mechanics *Nat. Commun.* 3 792
- [76] Fairbanks B D, Schwartz M P, Bowman C N and Anseth K S 2009 Photoinitiated polymerization of PEG-diacrylate with lithium phenyl-2,4,6-trimethylbenzoylphosphinate: polymerization rate and cytocompatibility *Biomaterials* 30 6702–7